Research Article | Vol. 31, No. 10 / 8 May 2023 / Optics Express 16393
Optics EXPRESS

Tolerance to aberration and misalignment in a two-point-resolving image inversion interferometer

DAVID J. SCHODT,[1,2,*] PATRICK J. CUTLER,[2] FRANCISCO E. BECERRA,[1,3] AND KEITH A. LIDKE[1]

[1]Department of Physics and Astronomy, University of New Mexico, Albuquerque, New Mexico, USA
[2]Teledyne Scientific & Imaging, LLC, USA
[3]Center for Quantum Information and Control, University of New Mexico, Albuquerque, New Mexico, USA
[*]david.schodt@teledyne.com

Abstract: Image inversion interferometry can measure the separation of two incoherent point sources at or near the quantum limit. This technique has the potential to improve upon current state-of-the-art imaging technologies, with applications ranging from microbiology to astronomy. However, unavoidable aberrations and imperfections in real systems may prevent inversion interferometry from providing an advantage for real-world applications. Here, we numerically study the effects of realistic imaging system imperfections on the performance of image inversion interferometry, including common phase aberrations, interferometer misalignment, and imperfect energy splitting within the interferometer. Our results suggest that image inversion interferometry retains its superiority to direct detection imaging for a wide range of aberrations, so long as pixelated detection is used at the interferometer outputs. This study serves as a guide for the system requirements needed to achieve sensitivities beyond the limits of direct imaging, and further elucidates the robustness of image inversion interferometry to imperfections. These results are critical for the design, construction, and use of future imaging technologies performing at or near the quantum limit of source separation measurements.

1. Introduction

The achievable resolution of any imaging system is directly related to its response to point sources in the image plane, which is characterized by the point spread function (PSF) [1,2]. The conventional limit for resolving two point sources, known as the Rayleigh limit, states that two sources are resolvable for separations greater than their diffraction-limited spot size [3,4]. The Cramér–Rao lower Bound (CRB) bounds the minimum variance attainable for an unbiased estimator. The quantum CRB (qCRB), however, bounds the minimum variance achievable by any measurement paired with any estimator. The qCRB for the separation between two incoherent point sources is, notably, independent of the source separation [5], suggesting that the Rayleigh limit is not a fundamental barrier to their resolution. Correspondingly, the Rayleigh limit has been circumvented by diverse imaging techniques, enabling resolution of two sources separated below the diffraction limit under certain conditions. For example, many super-resolution microscopy techniques circumvent the Rayleigh limit by taking advantage of some form of independence between the point sources, such as temporal independence [6–11], a combination of temporal and spatial independence [12], or spectral (color) independence [13], allowing independent localization of each source with sub-diffraction limit precision. In a complementary paradigm, modal imaging has the potential to provide unprecedented resolution of point sources and to approach the quantum limits in optical resolution [5]. Modal imaging performs a decomposition of the electromagnetic field from the point sources in a set of orthogonal spatial modes followed by photon detection onto these modes [5,14]. An appropriate choice of modal decomposition

#487808 https://doi.org/10.1364/OE.487808
Journal © 2023 Received 16 Feb 2023; revised 19 Apr 2023; accepted 19 Apr 2023; published 1 May 2023

Optics EXPRESS

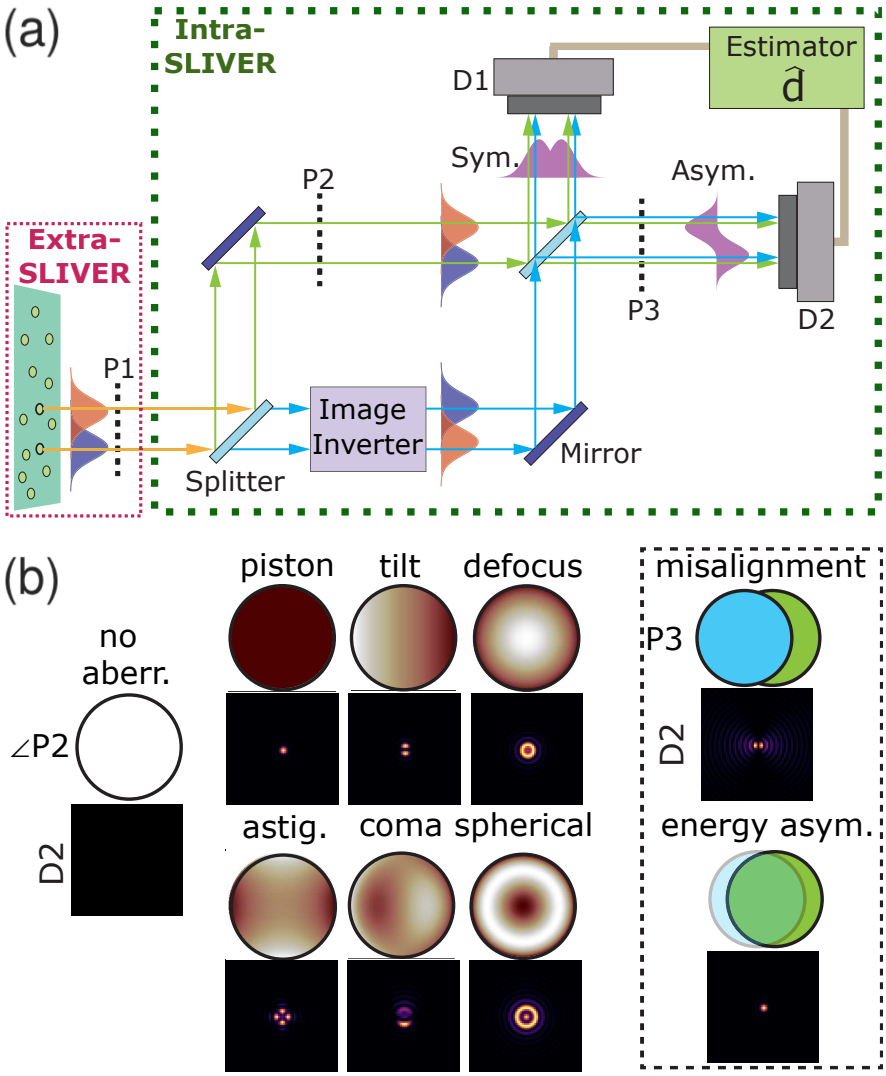

Fig. 1. SLIVER concept and aberrations. (a) Schematic for a SLIVER interferometer. P1 indicates a pupil plane at the interferometer entrance. P2 indicates a pupil plane within one arm of the interferometer. P3 indicates a pupil plane in the SLIVER anti-symmetric detection path. D1/D2 indicate single-photon sensitive sensors which detect the symmetric/anti-symmetric signals, respectively. Note that imaging lenses (e.g., converging lenses in front of the detectors) are excluded from the diagram. (b) Left: Illustrative examples of intra-SLIVER phase aberrations (simulated pupil phases ∠P2 are outlined by black circles) and the corresponding signals measured on D2 (simulated noiseless detections are shown as square images). Right, inside black dashed box: Illustrative examples of interferometer misalignment and energy asymmetry as they would present at pupil P3, with corresponding noiseless detections at D2 shown below each pupil illustration. Note that the blue and green pupils illustrating the energy asymmetry imperfection have differing transparencies, with spatial offsets included for visual distinction of the two pupils.

Optics EXPRESS

in principle allows for extracting the maximum amount of information per photon about the separation distance between point sources. For the problem of resolving two point sources with Gaussian PSFs, an optimal measurement that achieves the quantum limit consists of projections onto Laguerre-Gauss modes and photon counting [5]. Such measurement allows for resolving two point sources with precision independent of their separation [5]. The problem of resolving two point sources plays a central role in the study of protein-protein interactions in biophysics [15–17] and in the search for exoplanets in astronomy/astrophysics [18].

Recent advancements in optical field control have demonstrated spatial mode demultiplexers with complex optical setups [19–21]. On the other hand, there are simpler modal imaging setups that decompose the photon field into a small number of optical modes that can approach or even reach the qCRB for two-point source separation estimation [5,22–25]. Among these techniques, Super Localization by Image inVERsion interferometry (SLIVER) [22] decomposes the photon field into symmetric and anti-symmetric components. Photon counting onto these components allows for achieving the qCRB for resolving two point sources in the deep sub-Rayleigh regime. Such techniques can in principle be integrated with state-of-the-art imaging technologies for microscopy, astronomy, and target detection/pattern recognition, expanding their ability to resolve multiple sources. This integration, however, requires a deep understanding of how these measurements perform in imaging systems with realistic imperfections including aberrations, photon loss, background, detector noise, and intensity distortion.

In this article, we numerically investigate the performance of SLIVER in the presence of aberrations and imperfections relevant to practical complex imaging systems. In particular, we focus on the problem of separation estimation of two point sources with SLIVER in the presence of misalignment (misalignment of the two arms of the interferometer shown in Fig. 1(a)), imperfect energy splitting between the interferometer arms, and several common phase aberrations (piston, tilt, defocus, astigmatism, coma, and spherical). Our primary contributions made in this article are as follows:

- we quantify and compare the effects of several aberrations on SLIVER's ability to measure the separation between two point sources
- we investigate the benefits of using pixelated versus bucket detection at the outputs of a SLIVER interferometer
- we demonstrate the need to characterize and incorporate aberrations into imaging models used to estimate source separations from SLIVER data

2. Methods

2.1. SLIVER simulation

Figure 1(a) shows a schematic of the SLIVER interferometer used to measure the separation between two point sources (excluding imaging lenses used in, e.g., microscopy applications). The input field is split into two spatial modes $\psi_1(x, y)$ and $\psi_2(x, y)$ (corresponding to the fields in the two arms of the interferometer) with equal energy. The field $\psi_2(x, y)$ in one arm of the interferometer enters an image inversion system, transforming the field as $\psi_2(x, y) \rightarrow \psi_2(-x, -y)$. The two paths are then recombined by a 50/50 beamsplitter. The interference between these two fields allows for sorting the symmetric and anti-symmetric components of the input field, which are detected by single-photon sensitive detectors.

We consider a realistic SLIVER optical system where half of the energy is sent to a direct detection channel that could in principle be used to estimate the centroid of the emitter pair [26]. We note that the direct detection channel–which is excluded from Fig. 1(a)–would be picked off at pupil P1 with an additional beamsplitter. The remaining energy is then split equally between

Optics EXPRESS

the two arms of the interferometer. The electric field in each arm of the interferometer is defined in the spatial frequency domain (k_x, k_y) as

$$\tilde{\psi}_1(k_x, k_y) = |A_1(k_x, k_y)| \exp(i\Phi_1(k_x, k_y)) \tag{1}$$

$$\tilde{\psi}_2(k_x, k_y) = |A_2(k_x, k_y)| \exp(i\Phi_2(k_x, k_y))\text{MASK}(k_x, k_y) \tag{2}$$

where $|A(k_x, k_y)|$ is the real-valued amplitude of the field, $\Phi(k_x, k_y)$ is the real-valued phase, and $\text{MASK}(k_x, k_y)$ is a (complex-valued) pupil mask which we use to simulate field aberrations in one arm of the interferometer (i.e., a mask at pupil P2). The intensities at the symmetric and anti-symmetric outputs of the interferometer are then defined as

$$I_{\text{sym}} = \frac{1}{4}|\psi_1(x, y) + \psi_2(-x, -y)|^2 \tag{3}$$

$$I_{\text{asym}} = \frac{1}{4}|\psi_1(x, y) - \psi_2(-x, -y)|^2 \tag{4}$$

where $\psi(x, y) = \mathcal{F}\{\tilde{\psi}(k_x, k_y)\}$ denotes the field at the detector.

The two point sources were simulated by separating them symmetrically with respect to the SLIVER inversion point by a fixed distance along the horizontal (with respect to all images/aberrations shown) axis. We consider a constant and equal emission rate for each point source during the measurement period.

For the pixelated detectors, we sampled I_{sym} and I_{asym} by computing $\psi_1(x, y)$ and $\psi_2(x, y)$ at the center of each pixel, where we defined the pixel size $\delta x \equiv (\lambda/2n_a)/2\sqrt{2}$ to approximate Nyquist sampling of the signal along the pixel diagonal given emission wavelength $\lambda = 600$ nm and an effective numerical aperture of $n_a = 1.2$. We include a plot of the CRB with this simulated pixel size compared to that resulting from a pixel size reduced by a factor of four (i.e., $\delta x' = \delta x/4$) in Fig. S14. The close correspondence between the CRBs simulated with δx and $\delta x'$ suggests that our sampling scheme is sufficient to probe the underlying trends.

To investigate the advantages provided by pixelated SLIVER detection [27], we also simulated bucket detection [22] (i.e., the outputs of the interferometer are detected with a point detector) for the same interferometer setup used for pixelated detection. The bucket detectors were defined as the sum of the signal observed in the pixelated SLIVER detectors, with the direct detection channel remaining pixelated.

2.1.1. System aberrations and imperfections

In this work, we considered several common aberrations and imperfections: phase aberrations, interferometer misalignment, and imperfect splitting of the energy incident on the interferometer. We divided aberrations into two categories:

- **intra-SLIVER** aberrations, or aberrations within the interferometer (at either pupil P2 or P3 in Fig. 1(a))
- **extra-SLIVER** aberrations, or aberrations present at the entrance of the interferometer (at pupil P1 in Fig. 1(a))

We defined units of "aberration severity" such that 0 corresponds to no aberration and 1 corresponds to a severe aberration, with "severe" aberration defined below for each type of aberration investigated.

Common phase aberrations affecting the SLIVER interferometer were modeled by synthesizing $\text{MASK}(k_x, k_y)$ or $\Phi_1(k_x, k_y)$ and $\Phi_2(k_x, k_y)$ in the basis of Zernike polynomials and modifying the desired coefficients. For example, phase aberrations in ψ_2 were simulated by modifying the Zernike coefficients $c_{n,l}$ in $\angle\text{MASK}(k_x, k_y) = \sum_{n,l} c_{n,l} Z_n^l(k_x, k_y)$, where Z_n^l is the Zernike

Optics EXPRESS

polynomial of radial degree n and azimuthal degree l. We considered phase aberrations both within the interferometer itself (intra-SLIVER as previously defined) and external to the interferometer (extra-SLIVER). Intra-SLIVER phase aberrations were simulated as a mask in pupil P2 (see Fig. 1(a) and Eq. (2)) whereas extra-SLIVER phase aberrations were simulated in pupil P1 (by setting $\Phi_1 = \Phi_2 \neq 0$ in Eqs. (1) and (2)). The Zernike coefficients considered were chosen to span the range of no aberration ($c_{n,l} = 0$) to severe aberration ($c_{n,l} = 0.5$). For extra-SLIVER aberrations, which are attributable to the microscope or telescope attached to the SLIVER interferometer, our definition of severe aberration $c_{n,l} = 0.5$ reflects our own experience with microscopes (see also [28], which presents phase-retrieval results from several microscopes for which $|c_{n,l}| \lesssim 40 \times 10^{-3}\lambda \leftrightarrow |c_{n,l}| \lesssim 0.25$ radians). For intra-SLIVER aberrations, we again define severe aberration by $c_{n,l} = 0.5$, as this value is comparable to wavefront deviations resulting from the high-quality mirrors often used in optical interferometry (e.g., Thorlabs product #BB1-E02, whose surface flatness is roughly $\lambda/10 \leftrightarrow 0.6$ radians). Specific phase aberrations were oriented such that they generate the worst-case degradation of the SLIVER performance (e.g., tilt aberrations are simulated with the tilt varying along the axis of source separation).

Misalignment of the SLIVER interferometer was simulated by applying a phase gradient across the field $\psi_2(x, y)$ (i.e., a phase gradient at the detector is equivalent to an offset between the two arms of the interferometer). Misalignments were chosen ranging from no misalignment to a severe misalignment of 0.1 times the pupil radius. Our definition of severe misalignment was chosen by assuming a pupil radius of 2-5 mm, hence a severe misalignment would be 0.2-0.5 mm, which we consider to be the upper limit of misalignment that an experienced optical experimentalist might accept. All misalignments are oriented along the axis of source separation, representing the worst-case performance degradation for SLIVER.

Imperfect splitting of the field incident on the interferometer was simulated as an efficiency factor differentially splitting the total energy between the two arms of the interferometer, with the total energy entering the interferometer remaining fixed. That is, $|A_1(k_x, k_y)|$ and $|A_2(k_x, k_y)|$ were adjusted such that $|A_1(k_x, k_y)|^2 + |A_2(k_x, k_y)|^2 =$ constant. Intensity differences $|A_1(k_x, k_y)|^2 - |A_2(k_x, k_y)|^2$ ranging from 0% to 20% were selected to span the range of no asymmetry to the upper limit of what might be observed for a high quality beamsplitter.

Qualitative examples of the intra-SLIVER aberrations, interferometer misalignment, and energy asymmetry are shown in Fig. 1(b). For each of the intra-SLIVER aberrations, we plot the phase of the field at the circular pupil P2 (i.e., $\angle$P2 = Φ_2, where Φ_2 is the phase given in Eq. (2)) and the corresponding intensity at the square detector D2 (i.e., the intensity defined by Eq. (4)). For the interferometer misalignment example shown within the dashed box in Fig. 1(b), we illustrate qualitatively the misalignment as blue and green circles offset from one another, corresponding to spatial offsets of the fields defined by Eqs. (1)–(2). The corresponding intensity at square detector D2 is plotted underneath the illustration of the offset pupils. Similarly, imperfect splitting of the field incident on the interferometer ("energy asym.") is depicted by blue and green circles with differential transparencies (and spatially offset for visual effect) in the dashed box in Fig. 1(b), with the corresponding intensity at square detector D2 plotted underneath.

2.2. *Assessment of performance of the SLIVER system based on the Cramér–Rao lower bound*

To investigate the effects of aberrations on the SLIVER technique, we computed the CRB for estimating the source separation d in the presence of aberrations/misalignments. The CRB for estimating d in the presence of aberration provides a direct measure of the degradation in performance of SLIVER technique with respect to the ideal SLIVER measurement.

Optics EXPRESS

2.2.1. Classical Cramér–Rao lower bound

The CRB was computed numerically assuming unbiased estimators of the centroid μ, separation d, and intensity ratio q between the two point sources. Specifically, the CRB was computed assuming a Poisson noise model by numerically calculating the classical Fisher information matrix $I(\mu, d, q)$ at the true values of μ, d, and q and inverting the resulting 3x3 matrix. The CRB of the separation d between the two point sources is then given as

$$\sigma_d^2 = (I^{-1})_{2,2} \tag{5}$$

(i.e., the second diagonal element of the inverse of the Fisher information matrix).

2.2.2. Quantum Cramér–Rao lower bound

The qCRB was computed as described in [29] assuming a Gaussian PSF with standard deviation $\sigma_{\text{PSF}} = 0.21\lambda/n_a$ where λ is the central emission wavelength. This value of σ_{PSF} is that which minimizes the mean squared error of a Gaussian fit to the central lobe of the Airy PSF [30]. Specifically, we compute the qCRB as

$$\sigma_{\text{qCRB}}^2 = (Q^{-1})_{2,2} \tag{6}$$

where the quantum Fisher information matrix $Q(\mu, d, q)$ was computed from Eq. (10) in Ref. [29].

Notably, the CRB defined by Eq. (5) will be equal to the qCRB defined by Eq. (6) for a quantum optimal measurement of the two-point source separation when the underlying image formation models are equivalent. As such, the qCRB was used as a convenient scaling factor in several plots, although we emphasize that our estimate of the qCRB is for a Gaussian PSF, whereas our simulations used the scalar diffraction theory PSF (i.e., the Fourier transform of the pupil, which is the Airy PSF in the case of no aberrations).

2.3. Maximum likelihood estimate of d

Maximum likelihood estimates (MLE) $\hat{d}$ of d were obtained as follows. For a given aberration type, we computed the MLE in two scenarios: (1) from a model that includes knowledge of the type and strength of aberration present in the imaging system and (2) from a model that assumes an imaging system with no aberration. In other words, in scenario (1) we model the detected intensities at D1 and D2 (see Fig. 1(a)) as the intensities defined by Eqs. (3) and (4), respectively. In contrast, in scenario (2) we model the detected intensities by Eqs. (3) and (4) but with $\psi_1(x, y) = \psi_2(x, y)$, which models the intensity expected from an unaberrated SLIVER measurement. The models used in Fig. 3(a, b) did not include knowledge of the aberration, while the models used in Figs. 3(c, d) and S1-S13(b) incorporated the exact type and strength of aberration present.

The plots of $\hat{d}$ versus d shown in Figs. 3 and S1-S13(b) were generated by simulating $N_{\text{sim}} = 400$ aberrated measurements corrupted by Poisson noise and then minimizing the negative log-likelihood of the model using the Nelder-Mead method. Specifically, we compute the likelihood of a given model as follows. Given data $D = \{n_k\}$ corresponding to Poisson-noise corrupted photon counts observed at each pixel k of each detector, we have an intensity model $I(d) = \{\mu_k(d)\}$ of the expected photon count at those same pixels. For each simulation, the likelihood was then computed as

$$\mathcal{L}(d|D) = \prod_k \frac{\mu_k(d)^{n_k} \exp(-\mu_k(d))}{n_k!} \tag{7}$$

and the MLE of the source separation was computed as

$$\hat{d} = \underset{d}{\text{argmin}} \left(-\log \mathcal{L}(d|D)\right) \tag{8}$$

Optics EXPRESS

The final value of $\hat{d}$ was then generated by averaging over the N_{sim} estimators as $\hat{d} \equiv \sum_{n=1}^{N_{\text{sim}}} \hat{d}_n / N_{\text{sim}}$.

2.4. Interference visibility

For practical applications in imaging using inversion interferometry, the interference visibility [31] is an accessible measurement that can provide us with information about the level of aberration within the interferometer. We computed the visibility of the SLIVER interferometer for each simulated aberration by performing a phase sweep from 0 to 2π across one arm of the interferometer for a source separation of $d = 0$ (i.e., by sweeping $\Phi_2 \rightarrow \Phi_2 + 2\pi$ with Φ_1 fixed in Eqs. (1)–(2)). The visibility was then computed as

$$V = \frac{I_{\text{max}} - I_{\text{min}}}{I_{\text{max}} + I_{\text{min}}} \tag{9}$$

where I_{min} and I_{max} are the minimum and maximum observed intensities, respectively.

3. Results and discussion

Common aberrations were simulated as described in Sec. 2.1. For each aberration, we computed both the visibility and σ_d (the square root of the CRB for estimating the source separation d) as a function of increasing aberration for a SLIVER interferometer with either pixelated detection or with bucket detection of its outputs. We additionally compared σ_d for the SLIVER measurement of two sources separated by $\sigma_{\text{PSF}}/10$ to the bound obtained for a purely direct detection measurement, whereby all photons were diverted to the direct detection channel.

As a further study, we investigated the bias of the MLE $\hat{d}$ of the source separation d in the presence of aberration. As described in Section 2.3, we performed this experiment in two scenarios: (1) when the model incorporates knowledge of the type and strength of the underlying aberration, and (2) when the model assumes no aberration. For the models incorporating knowledge of the underlying aberration, we additionally compute the MLE at different levels of detected signal.

We highlight key results from each of these experiments in Figs. 2–4, and in the following sections we present and discuss these results in detail.

3.1. Interference visibility

The degradation in visibility (Eq. (9)) due to intra-SLIVER aberration is shown in Fig. 2(a) for each of the intra-SLIVER aberrations investigated. Interestingly, all intra-SLIVER phase aberrations considered except piston (tilt, defocus, astigmatism, coma, and spherical phase aberrations) have a nearly identical effect on the visibility. The pupil misalignment and intensity asymmetry aberrations both have limited impacts on visibility as compared to the phase aberrations considered.

Of the extra-SLIVER phase aberrations considered, only tilt and comatic aberrations affect the visibility (see Fig. 2(b)).

3.2. Cramér–Rao lower bound

For each aberration, we computed σ_d, the square root of CRB for estimating the two-source separation for an aberrated SLIVER interferometer with either pixelated or bucket detection at its outputs. We scaled σ_d by σ_{qCRB} (the square root of the qCRB for the corresponding Gaussian PSF [29]) to benchmark the degradation in performance of the SLIVER technique in the presence of aberrations. The CRB with pixelated detection versus aberration severity is shown in Fig. 2(c) for intra-SLIVER aberrations and in Fig. 2(d) for extra-SLIVER aberrations. Overall, most of

Optics EXPRESS

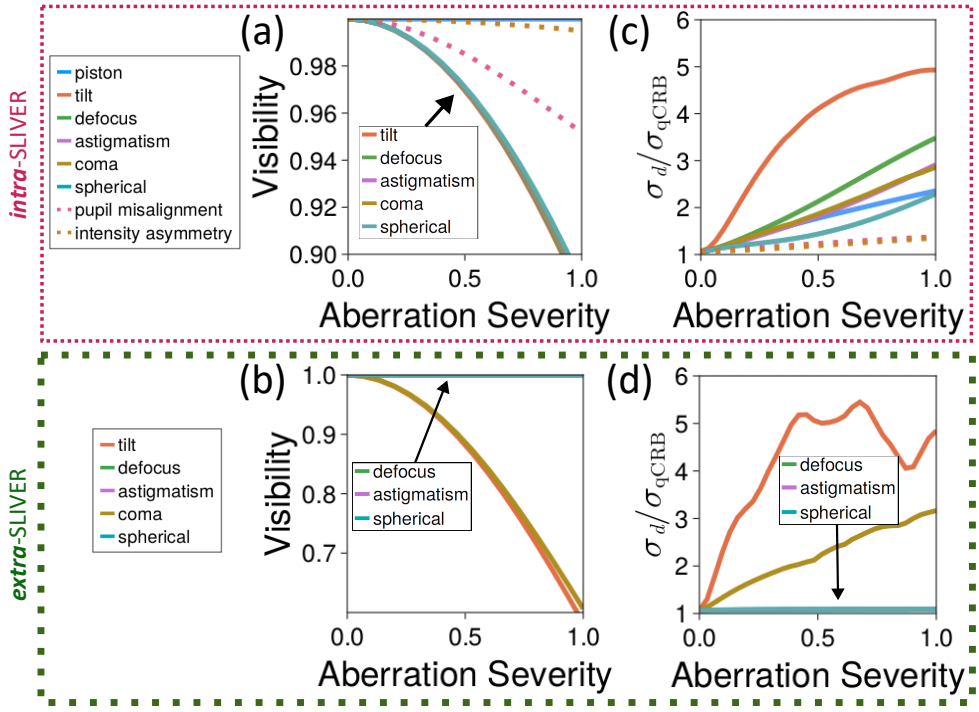

Fig. 2. Effects of aberrations on visibility and estimation precision of source separation. Estimation precision of source separation is defined as $\sigma_d = \sqrt{\mathrm{CRB}}$. (a, b) SLIVER interferometer visibility as a function of the "aberration severity" unit for (a) intra-SLIVER aberrations (i.e., aberrations at pupils P2 or P3 in Fig. 1(a)) and (b) extra-SLIVER aberrations (i.e., aberrations at pupil P1 in Fig. 1(a)). (c, d) $\sigma_d/\sigma_{\mathrm{qCRB}}$ for SLIVER with pixelated detection as a function of increasing aberration severity for a two source separation of $d = \sigma_{\mathrm{PSF}}/10$ for (c) intra-SLIVER and (d) extra-SLIVER aberrations.

the aberrations investigated tend to degrade the precision bound in a predictable, roughly linear manner with increasing aberration severity within the range of severity considered.

The CRB versus increasing aberration severity is shown for each aberration in Figs. 2(c, d) and S1-S13(a). Focusing on individual aberrations, phase tilt aberrations have the greatest negative impact on overall SLIVER performance. The negative impact of a tilt aberration is expected since the lowest order anti-symmetric mode contains the most information about the source separation, and tilt is the lowest order anti-symmetric aberration. Looking at Figs. 2(c, d), S2, and S7, we see that σ_d increases steeply in the presence of either intra- or extra-SLIVER tilt aberration, emphasizing that special care should be taken to reduce phase tilt both within a SLIVER interferometer and at its entrance.

Extra-SLIVER aberrations (i.e., those attributable to a system attached to the SLIVER interferometer) have a more varied influence on SLIVER performance in comparison to intra-SLIVER aberrations. For radially symmetric extra-SLIVER phase aberrations, such as defocus or spherical aberration, the effect is negligible (see Figs. 2(d), S8-S9(a), and S11(a)), as the interferometer arm realizing image inversion will still generate a complementary field to cancel the unperturbed field when combined in the anti-symmetric channel. In contrast, for extra-SLIVER aberrations with little to no radial symmetry (e.g., tilt or coma), the degradation in SLIVER performance is dramatic (see Figs. 2(d), S7(a), and S10(a)), as after image inversion such aberrations are roughly comparable to having twice as much aberration in one arm of

Optics EXPRESS

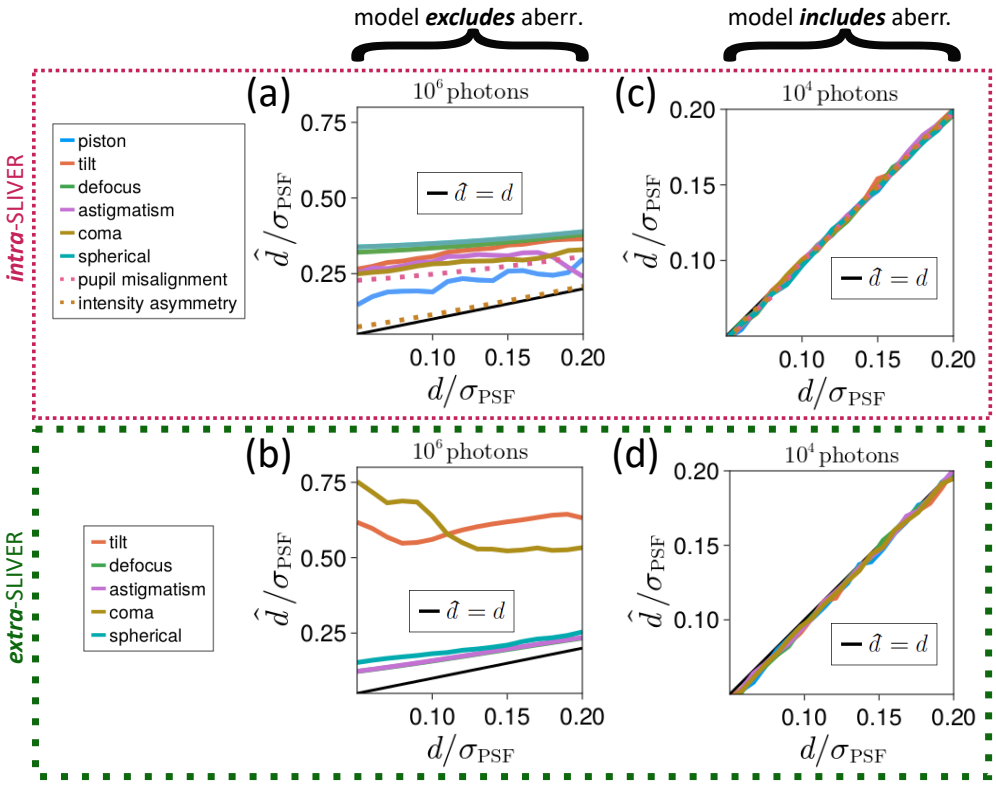

Fig. 3. Effects of aberrations on estimation bias of source separation. Estimation bias is defined as $\hat{d} - d$. (a, b) MLE $\hat{d}$ of the source separation d when the model does not account for the aberration for (a) intra-SLIVER aberrations (i.e., aberrations at pupils P2 or P3 in Fig. 1(a)) and (b) extra-SLIVER aberrations (i.e., aberrations at pupil P1 in Fig. 1(a)). (c, d) MLE $\hat{d}$ of the source separation d when the model accounts for the exact type and strength of aberration for (c) intra-SLIVER aberrations (i.e., aberrations at pupils P2 or P3 in Fig. 1(a)) and (d) extra-SLIVER aberrations (i.e., aberrations at pupil P1 in Fig. 1(a)). The results shown in (a, b) correspond to 10^6 collected photons, while the results shown in (c, d) correspond to only 10^4 collected photons. An aberration severity of 0.5 was used for all aberrations investigated. All results correspond to pixelated detection of the SLIVER outputs.

the interferometer. These results suggest that if a SLIVER interferometer is to be integrated with an existing microscope/telescope, special care must be taken to reduce radially asymmetric aberrations in the microscope/telescope.

3.2.1. Pixelated versus bucket detection of SLIVER outputs

The CRB of the separation versus aberration severity for both pixelated and bucket detection SLIVER is shown in Figs. S1-S13(a), with pixelated detection indicated by solid lines and bucket detection by dashed lines. For all aberrations and imperfections investigated, pixelated detection at the outputs of the SLIVER system substantially outperforms bucket detection. For some aberrations, pixelated detection allows for separation estimates reasonably close to the quantum limit, while bucket detection fails dramatically. For example, when measuring a separation of $d = \sigma_{\mathrm{PSF}}/20$ in the presence of an interferometer arm misalignment of 0.05 pupil radii, σ_d for bucket detection is nearly six times the quantum limit, while σ_d for pixelated detection is only

Optics EXPRESS

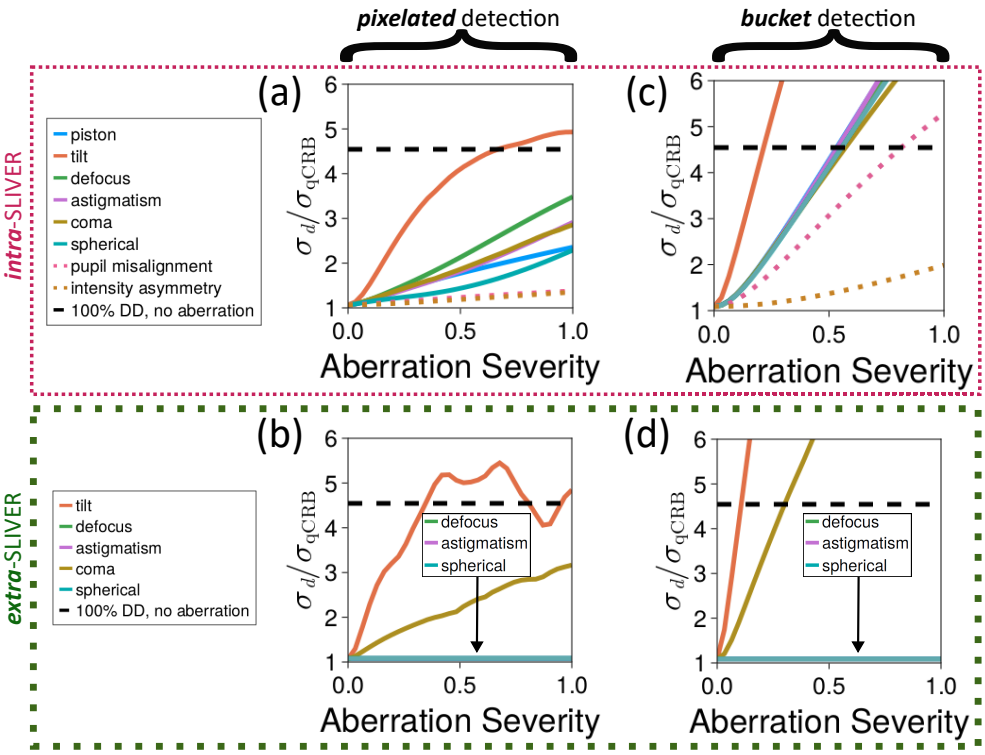

Fig. 4. Aberration severity beyond which SLIVER may not provide a benefit. (a, b) Separation CRB for a pixelated SLIVER measurement versus aberration severity compared to the separation CRB obtained from an unaberrated, pure direct detection measurement (black dashed line) for (a) intra-SLIVER and (b) extra-SLIVER aberrations. (c, d) Separation CRB for a bucket SLIVER measurement versus aberration severity compared to the separation CRB obtained from an unaberrated, pure direct detection measurement (black dashed line) for (c) intra-SLIVER and (d) extra-SLIVER aberrations. All values of σ_d were computed for a source separation of $\sigma_{\mathrm{PSF}}/10$.

minimally affected (see Fig. S12(a)). As such, single photon sensitive pixelated detection is likely necessary for most practical and precise applications of SLIVER.

To further emphasize the benefits of pixelated SLIVER – and of the SLIVER technique in general – we compare σ_d for both pixelated and bucket detection SLIVER to the separation CRB obtained for an unaberrated, purely direct detection measurement of two sources separated by $\sigma_{\mathrm{PSF}}/10$ in Fig. 4. With pixelated detection, all aberrations except tilt permit a lower CRB than the purely direct detection measurement within the range of aberration severity considered (see Fig. 4(a, b)). In contrast, the CRB for bucket detection SLIVER exceeds that of the unaberrated direct detection measurement for several aberrations within the range of aberration severity considered (see Fig. 4(c, d)). These results suggest that SLIVER with pixelated detection is a robust tool for measuring sub-Rayleigh limit separations between two point sources, as it retains a benefit over a perfect (unaberrated) direct detection measurement even for severe levels of aberration in the SLIVER system.

3.3. Maximum likelihood estimate of d

MLE estimates of the source separation d were computed as described in Section 2.3. The MLE using a model ignorant to the underlying aberration is summarized for aberrations isolated to

Optics EXPRESS

one arm of the interferometer in Fig. 3(a) and for aberrations at the interferometer entrance in Fig. 3(b). For individual aberrations, the MLE from the model incorporating knowledge of the aberration is shown at varying signal levels in Figs. 3(c, d) and S1-S13(b).

For most aberrations and system imperfections considered, the MLE $\hat{d}$ of the source separation d was biased towards overestimating the separation when the model did not account for the aberration (see Fig. 3(a, b)). Furthermore, as shown in Fig. 3(a, b), the bias of the estimator was well beyond what might be considered acceptable when the model does not account for the aberration, even for the relatively large number of photons collected (10^6). In contrast, the bias of the estimator was typically minimal and followed predictable trends (with respect to separation and total photons measured) when the model incorporated knowledge of the specific aberration (see Figs. 3(c, d) and S1-S13(b)). As such, the bias of the MLE is likely less consequential than an increased CRB of separation estimates, so long as one is able to characterize the aberrations and include their effects in the model. For example, phase aberrations can be well-characterized without the need for specialized hardware [32,33]. Similarly, asymmetric energy splitting by the beamsplitters, which itself is relatively inconsequential, can be well-characterized to within <5% by standard, low-precision optical power meters. Overall, these results suggest that aberrations should be well-characterized after alignment of a SLIVER system and accounted for during data analysis.

4. Conclusion

In this study, we numerically investigated the degradation of two source separation estimates by SLIVER in the presence of optical aberrations and imperfections commonly encountered in microscopy and interferometry. We have shown that the performance of a SLIVER system with bucket detectors at its outputs rapidly degrades in the presence of even minor aberrations within or at the entrance to the SLIVER interferometer. We have shown, in contrast, that a pixelated SLIVER measurement (i.e., detecting the symmetric and anti-symmetric SLIVER outputs with single-photon sensitive array detectors) is relatively robust to aberration, with pixelated SLIVER being superior to a purely direct detection measurement alone for nearly all aberrations considered. In particular, we have shown that a pixelated SLIVER measurement of the separation is superior to a direct detection measurement for all intra-SLIVER aberrations (i.e., aberrations within the interferometer) investigated except for phase tilt, suggesting that special care must be taken to reduce phase tilt aberration within the SLIVER interferometer. We have shown that radially symmetric aberrations present at the entrance of the SLIVER optical system have little effect on its ability to resolve the separation between two sources, while radially asymmetric aberrations can be especially deleterious to SLIVER performance. These results emphasize the importance of careful alignment of the optical system to which a SLIVER interferometer is attached, ensuring, for example, that collected light hits relevant optical interfaces at perpendicular angles (e.g., in the context of microscopy, radially asymmetric aberrations often result from hitting diffractive optical elements, such as lenses, at non-perpendicular angles) and that the optical system is well-aligned to the interferometer. Finally, we have shown that the bias of the MLE of the separation from pixelated SLIVER data is minimal and rather predictable when our model incorporates knowledge of the aberrations plaguing the optical system. In summary, our results demonstrate that SLIVER is a robust tool for measuring sub-Rayleigh separations between two sources beyond the limits of direct detection so long as

- care is taken to reduce phase tilt aberration within the interferometer
- radially asymmetric phase aberrations, such as tilt or coma, are minimal in the optical system (e.g., microscope or telescope) to which the SLIVER interferometer is attached
- the outputs of the SLIVER interferometer are measured by pixelated detectors

Optics EXPRESS

- remaining aberrations are well-characterized and accounted for in analysis

Funding. National Science Foundation (2039517); National Institutes of Health (1R01GM140284); Defense Advanced Research Projects Agency (HR00112090127).

Acknowledgments. Approved for public release; distribution is unlimited.

Disclosures. DJS and PJC: Teledyne Scientific & Imaging, LLC (E)

Data availability. No data were generated or analyzed in the presented research.

Supplemental document. See Supplement 1 for supporting content.

References

1. W. E. Moerner, "Nobel lecture: Single-molecule spectroscopy, imaging, and photocontrol: Foundations for super-resolution microscopy," Rev. Mod. Phys. **87**(4), 1183–1212 (2015).
2. S. W. Hell, "Far-field optical nanoscopy," Science **316**(5828), 1153–1158 (2007).
3. Rayleigh, "XXXI. Investigations in optics, with special reference to the spectroscope," (1879).
4. M. Born and E. Wolf, *Principles of Optics*, 7th Edition (Cambridge University Press, 1999).
5. M. Tsang, R. Nair, and X.-M. Lu, "Quantum theory of superresolution for two incoherent optical point sources," Phys. Rev. X **6**(3), 031033 (2016).
6. K. A. Lidke, B. Rieger, T. M. Jovin, and R. Heintzmann, "Superresolution by localization of quantum dots using blinking statistics," Opt. Express **13**(18), 7052–7062 (2005).
7. M. J. Rust, M. Bates, and X. Zhuang, "Sub-diffraction-limit imaging by stochastic optical reconstruction microscopy (STORM)," Nat. Methods **3**(10), 793–796 (2006).
8. E. Betzig, R. Sougrat, O. W. Lindwasser, S. Olenych, J. S. Bonifacino, M. W. Davidson, J. Lippincott-schwartz, and H. F. Hess, "Imaging Intracellular Fluorescent Proteins at Nanometer Resolution," Science **313**(5793), 1642–1645 (2006).
9. S. T. Hess, T. P. Girirajan, and M. D. Mason, "Ultra-high resolution imaging by fluorescence photoactivation localization microscopy," Biophys. J. **91**(11), 4258–4272 (2006).
10. M. Heilemann, S. Van De Linde, M. Schüttpelz, R. Kasper, B. Seefeldt, A. Mukherjee, P. Tinnefeld, and M. Sauer, "Subdiffraction-resolution fluorescence imaging with conventional fluorescent probes," Angew. Chem., Int. Ed. **47**(33), 6172–6176 (2008).
11. R. Jungmann, C. Steinhauer, M. Scheible, A. Kuzyk, P. Tinnefeld, and F. C. Simmel, "Single-molecule kinetics and super-resolution microscopy by fluorescence imaging of transient binding on DNA origami," Nano Lett. **10**(11), 4756–4761 (2010).
12. S. W. Hell and J. Wichmann, "Breaking the diffraction resolution limit by stimulated emission: stimulated-emission-depletion fluorescence microscopy," Opt. Lett. **19**(11), 780–782 (1994).
13. S. Niekamp, J. Sung, W. Huynh, G. Bhabha, R. D. Vale, and N. Stuurman, "Nanometer-accuracy distance measurements between fluorophores at the single-molecule level," Proc. Natl. Acad. Sci. **116**(10), 4275–4284 (2019).
14. M. Tsang, "Subdiffraction incoherent optical imaging via spatial-mode demultiplexing," New J. Phys. **19**(2), 023054 (2017).
15. S. T. Low-Nam, K. A. Lidke, P. J. Cutler, R. C. Roovers, P. M. Van Bergen En Henegouwen, B. S. Wilson, and D. S. Lidke, "ErbB1 dimerization is promoted by domain co-confinement and stabilized by ligand binding," Nat. Struct. Mol. Biol. **18**(11), 1244–1249 (2011).
16. C. C. Valley, D. J. Arndt-Jovin, N. Karedla, M. P. Steinkamp, A. I. Chizhik, W. S. Hlavacek, B. S. Wilson, K. A. Lidke, and D. S. Lidke, "Enhanced dimerization drives ligand-independent activity of mutant epidermal growth factor receptor in lung cancer," Mol. Biol. Cell **26**(22), 4087–4099 (2015). PMID: 26337388.
17. C. Franco Nitta, E. W. Green, E. D. Jhamba, J. M. Keth, I. Ortiz-Caraveo, R. M. Grattan, D. J. Schodt, A. C. Gibson, A. Rajput, K. A. Lidke, B. S. Wilson, M. P. Steinkamp, and D. S. Lidke, "EGFR transactivates RON to drive oncogenic crosstalk," eLife **10**, e63678 (2021).
18. Z. Huang and C. Lupo, "Quantum hypothesis testing for exoplanet detection," Phys. Rev. Lett. **127**(13), 130502 (2021).
19. P. Boucher, C. Fabre, G. Labroille, and N. Treps, "Spatial optical mode demultiplexing as a practical tool for optimal transverse distance estimation," Optica **7**(11), 1621–1626 (2020).
20. N. K. Fontaine, R. Ryf, H. Chen, D. T. Neilson, K. Kim, and J. Carpenter, "Laguerre-gaussian mode sorter," Nat. Commun. **10**(1), 1865 (2019).
21. L. R. Hofer, L. W. Jones, J. L. Goedert, and R. V. Dragone, "Hermite–gaussian mode detection via convolution neural networks," J. Opt. Soc. Am. A **36**(6), 936–943 (2019).
22. R. Nair and M. Tsang, "Interferometric superlocalization of two incoherent optical point sources," Opt. Express **24**(4), 3684–3701 (2016).
23. W.-K. Tham, H. Ferretti, and A. M. Steinberg, "Beating rayleigh's curse by imaging using phase information," Phys. Rev. Lett. **118**(7), 070801 (2017).
24. Z. S. Tang, K. Durak, and A. Ling, "Fault-tolerant and finite-error localization for point emitters within the diffraction limit," Opt. Express **24**(19), 22004–22012 (2016).

Optics EXPRESS

25. F. Yang, A. Tashchilina, E. S. Moiseev, C. Simon, and A. I. Lvovsky, "Far-field linear optical superresolution via heterodyne detection in a higher-order local oscillator mode," Optica **3**(10), 1148–1152 (2016).
26. In our simulation, we placed the SLIVER inversion axis at the centroid of the emitter pair.
27. R. Nair and M. Tsang, "Far-field superresolution of thermal electromagnetic sources at the quantum limit," Phys. Rev. Lett. **117**(19), 190801 (2016).
28. R. Thorsen, C. N. Hulleman, M. Hammer, D. Grünwald, S. Stallinga, and B. Rieger, "Impact of optical aberrations on axial position determination by photometry," Nat. Methods **15**(12), 989–990 (2018).
29. J. Řehaček, Z. Hradil, B. Stoklasa, M. Paúr, J. Grover, A. Krzic, and L. L. Sánchez-Soto, "Multiparameter quantum metrology of incoherent point sources: Towards realistic superresolution," Phys. Rev. A **96**(6), 062107 (2017).
30. B. Zhang, J. Zerubia, and J.-C. Olivo-Marin, "Gaussian approximations of fluorescence microscope point-spread function models," Appl. Opt. **46**(10), 1819–1829 (2007).
31. F. L. Pedrotti, L. M. Pedrotti, and L. S. Pedrotti, *Introduction to Optics* (Cambridge University Press, 2017).
32. B. M. Hanser, M. G. L. Gustafsson, D. A. Agard, and J. W. Sedat, "Phase-retrieved pupil functions in wide-field fluorescence microscopy," J. Microsc. **216**(1), 32–48 (2004).
33. S. Liu, E. B. Kromann, W. D. Krueger, J. Bewersdorf, and K. A. Lidke, "Three dimensional single molecule localization using a phase retrieved pupil function," Opt. Express **21**(24), 29462–29487 (2013).